nature chemistry

Article

Solid solvation structure design improves all-solid-state organic batteries

Yang Hu [1,9], Han Su [1,2,9], Jiamin Fu [1,9], Jing Luo[1], Qihang Yu[3], Feipeng Zhao[1], Weihan Li [1,4,5], Sixu Deng [1,3], Yu Liu[1,2], Yi Yuan[1], Yi Gan [1], Yijia Wang[1], Jung Tae Kim[1], Ning Chen[6], Mohsen Shakouri [6], Xiaoge Hao[1], Yingjie Gao[1], Tianlu Pang[7], Nian Zhang [7], Ming Jiang[8], Xia Li [3], Yang Zhao [1], Jiangping Tu[2], Changhong Wang [1,4,5] ✉ & Xueliang Sun [1,4,5] ✉

Organic electrode materials offer a versatile, sustainable approach for next-generation lithium-ion batteries but are limited by low working voltages and poor cycling stability. Here we report a solid-solvation-structure design strategy to improve both the voltage and stability of organic electrode materials in all-solid-state batteries. As a proof of concept, we incorporate halide electrolytes as solid solutes and tetrachloro-*o*-benzoquinone as a solid solvent to form homogeneous solid cathode solutions. Systematic optimization of the inner solvation configuration enables tetrachloro-*o*-benzoquinone to achieve a high working voltage (3.6 V vs. Li⁺/Li) at room temperature within an asymmetric solid solvation sheath. Moreover, the equilibrium redox pathway and electrostatically driven self-healing interfaces revealed rapid redox kinetics and stable performance over 7,500 cycles in all-solid-state batteries under low stack pressures. This work demonstrates that organic electrode materials can serve as viable, durable and cost-effective alternatives to transition metal oxides in all-solid-state batteries.

Organic electrode materials (OEMs) have garnered significant research attention due to their versatile structures, cost-effectiveness and environmental sustainability[1–4]. Over the past decades, numerous OEMs have been explored for electrochemical energy storage, which can be generally classified into two categories: p-type (dual-ion mechanism) OEMs and n-type (rock-chair mechanism) OEMs[5,6]. p-Type OEMs, exemplified by conducting polymers such as polyaniline and polythiophene, are notable for their redox chemistry involving lone-pair electrons, resulting in a high average working voltage[7]. However, p-type OEMs face practical challenges, including large structural distortions due to the

(de)intercalation of anions with large radii, the necessity for customized electrolytes in dual-ion batteries and limited redox activity[8]. On the other hand, typical n-type OEMs, such as quinone derivatives with carbonyl redox chemistry, exhibit excellent reversibility and structural stability, making them strong candidates for practical applications[9]. Despite these advantages, long-standing challenges, which include low working voltages (mostly <3 V) when compared with transition metal oxides (TMOs; for example, LiCoO₂, LiNi_xMn_yCo_{1-x-y}O₂ and so on) and poor cycling stability due to severe dissolution in liquid electrolytes, have limited the widespread application of n-type OEMs so far[10,11].

[1]Department of Mechanical and Materials Engineering, University of Western Ontario, London, Ontario, Canada. [2]School of Materials Science and Engineering, Zhejiang University, Hangzhou, People's Republic of China. [3]Department of Chemical and Materials Engineering, Concordia University, Montreal, Quebec, Canada. [4]Eastern Institute for Advanced Study, Eastern Institute of Technology, Nngbo, People's Republic of China. [5]Zhejiang Key Laboratory of All-Solid-State Battery, Ningbo Key Laboratory of All-Solid-State Battery, Ningbo, People's Republic of China. [6]Canadian Light Source Inc., University of Saskatchewan, Saskatoon, Saskatchewan, Canada. [7]Shanghai Synchrotron Radiation Facility, Shanghai Advanced Research Institute, Chinese Academy of Sciences, Shanghai, People's Republic of China. [8]Institute of Physical Science and Information Technology, Anhui University, Hefei, People's Republic of China. [9]These authors contributed equally: Yang Hu, Han Su, Jiamin Fu. ✉e-mail: cwang@eitech.edu.cn; xsun@eitech.edu.cn

Over the past decades, extensive efforts have been devoted to addressing these challenges[12,13]. Typical strategies to elevate the working voltage include incorporating electron-withdrawing functional groups[13], leveraging charge delocalization by sacrificial metals[14] and designing mesomeric structures or exploring new redox chemistry beyond the typical enolate–carbonyl paradigm[15,16]. Meanwhile, efforts to mitigate the dissolution of n-type OEMs in liquid electrolytes have focused on polymerization[17–19], expanding the conjugation area[20,21] and synthesizing organic salts[22,23]. However, these strategies rarely converge, making it difficult to simultaneously achieve both a high working voltage and long-term cycling stability in full cells[5,24].

In this Article we introduce a solid-solvation-structure design strategy that enables both high working voltages and long-term cycling stability for n-type OEMs in all-solid-state batteries (ASSBs) (Supplementary Fig. 1). Using halide electrolytes as solid solutes and tetrachloro-o-benzoquinone (o-TCBQ) as a solid solvent to construct solid cathode solutions (Supplementary Figs. 2–4 and Supplementary Table 1), the working voltage of o-TCBQ can be effectively tuned. The in situ formation of an organic–inorganic network within these solid cathode solutions promotes an exceptional rate capability and cycling performance under a low stack pressure (≈7 MPa) at room temperature (RT). In the following sections, we systematically investigate the optimization of inner solvation structures, the impact of solvation evolution on the working voltage of o-TCBQ, the underlying redox chemistry and the mechanism of dynamically improved interfaces during cycling. These findings offer a pathway towards practical high-voltage, long-life OEMs and provide valuable insights for developing cost-effective, high-performance ASSBs.

Evolution of the solid solvation structure

Using two typical halide electrolytes Li_3InCl_6 and Li_2ZrCl_6, we observed distinct electrochemical behaviours of o-TCBQ after careful optimization of the cathode composites (Supplementary Figs. 5 and 6). Galvanostatic charge–discharge profiles show that cells using Li_2ZrCl_6 exhibit an ~0.2 V higher voltage compared with those using Li_3InCl_6 or conventional liquid electrolytes (Fig. 1a). This voltage enhancement is related to the dissolution of Zr^{4+} cations and the limited solubility of In^{3+} cations in the o-TCBQ solvent (Supplementary Figs. 7 and 8), as explained by Lewis acid–base theory[25,26]. To further explain the mechanism, we synthesized a series of $Li_{3-x}In_{1-x}Zr_xCl_6$ solid electrolytes and found that increasing the Zr^{4+} content gradually elevates the average working voltage of the o-TCBQ solvent (Fig. 1a and Supplementary Figs. 9 and 10). Whereas Li^+ ions are also soluble in the o-TCBQ solvent, this does not affect our analysis as they are released during subsequent charging[27]. To correlate such voltage increments with Zr^{4+} concentration, we define the relative working voltage increment η ($\eta = (V_{current} - V_{LIC})/(V_{LZC} - V_{LIC})$), where $V_{current}$ is the working voltage of the o-TCBQ solvent at a given Zr^{4+} concentration and V_{LIC} and V_{LZC} are the working voltages for Li_3InCl_6 and Li_2ZrCl_6, respectively. A solid-solvation-structure evolution model is proposed to relate η to the relative molar ratio of Zr^{4+} to In^{3+} cations (denoted as the R value) in $Li_{3-x}In_{1-x}Zr_xCl_6$ cathode solutions (Fig. 1b). At low R values ($R \ll 1$), o-TCBQ forms chelate complexes with the Zr^{4+} cation in the inner solvation sheath, with Cl^- anions positioned in the outer solvation sheath. This structure, termed the cation–solvent aggregate (CSA), features the polarization of a single Zr^{4+} cation shared among multiple o-TCBQ solvent molecules. In the CSA region, η is expected to show a linear correlation with increasing R value due to the continued coordination of Zr^{4+} cations with free o-TCBQ solvent molecules. As the Zr^{4+} concentration in increased to an R value of unity, Cl^- anions gradually enter the inner solvation sheath, leading to the formation of heteroleptic complexes. This structure, termed the contact cation–solvent pair (CCSP), can be viewed as a monomeric $ZrCl_4$ unit paired with an o-TCBQ solvent molecule. With a further increase in the Zr^{4+} concentration ($R > 1$) up to the solubility limit, the inner solvation sheath becomes predominantly occupied by Zr^{4+} cations and Cl^- anions, eventually forming binuclear heteroleptic

complexes. This final structure, termed the anion-separated cation–solvent pairs (ASCSP), features each o-TCBQ solvent molecule polarized by two Zr^{4+} cations, contributing to the highest achievable working voltage. A comparison with theoretical curves (Fig. 1b; Methods) shows that the experimental data align closely with the eight-coordinated CSA model (Supplementary Fig. 11).

The solid-solvation-structure evolution model is supported using various characterization methods. X-ray diffraction (XRD) patterns reveal that the pristine trigonal structure ($P\bar{3}m1$ space group) of the $Li_{2.25}In_{0.25}Zr_{0.75}Cl_6$ solid electrolyte transforms to a monoclinic phase ($C2/m$ space group), identical to that of Li_3InCl_6, after dissolution in o-TCBQ (Fig. 1c)[28,29]. In this context, the formation of a solid cathode solution via Zr^{4+} dissolution modulates the working voltage of o-TCBQ, while the remaining Li–In–Cl species play a critical role in facilitating rapid Li^+ transportation (Supplementary Fig. 12). This in-situ-formed organic–inorganic network promotes an exceptional electrochemical performance, which will be discussed later. Similarly, dissolving other $Li_{3-x}In_{1-x}Zr_xCl_6$ solid electrolytes into o-TCBQ also leads to attenuated XRD patterns compared with their pristine counterparts (Fig. 1c and Supplementary Fig. 13). A comparison of the Zr K-edge X-ray absorption near-edge structure (XANES) spectra of $ZrCl_4$, ZrO_2, $Li_{3-x}In_{1-x}Zr_xCl_6$ solid electrolytes and their corresponding cathode solutions shows key structural insights (Fig. 1d and Supplementary Fig. 14). At low R values ($x = 0.1$; $R = 0.2$), the dominant feature 'b', which belongs to the $1s \rightarrow 5p$ transition of Zr atoms, closely resembles the excitation of ZrO_7 pentagonal bipyramids in ZrO_2. At intermediate R values ($x = 0.25/0.5$; $R = 0.5/1.1$), new features 'a' and 'c' emerge, resembling the excitation behaviour of $ZrCl_6$ octahedra in $ZrCl_4$, indicating the progressive substitution of O by Cl surrounding the Zr^{4+} cations (the inner solvation sheath). At higher R values (x = 0.75/1; R = 1.7/2.3), the features 'a', 'b' and 'c' in the cathode solutions converge with those of the $Li_{3-x}In_{1-x}Zr_xCl_6$ solid electrolytes, indicating that Zr–Cl interactions dominate the inner solvation sheath at elevated Zr^{4+} concentrations. This evolution is further supported by similar trends observed in the pre-edge features of Cl K-edge X-ray absorption spectroscopy (XAS) and Zr K-edge extended X-ray absorption fine structure (EXAFS) spectra (Supplementary Figs. 15 and 16). Raman spectra show that the peaks corresponding to the asymmetric stretching vibration of the $ZrCl_6$ octahedra in $ZrCl_4$ disappear upon the formation of Zr^{4+}-based cathode solutions, accompanied by the emergence of a new peak group (P1) associated with solvated Zr–Cl interactions (Fig. 1e), confirming the dissolution of Zr^{4+} cations in o-TCBQ. Concurrently, the peaks related to the asymmetric stretching of C=O double bonds exhibit a redshift, with peak 'a' intensifying and peak 'c' diminishing as the R value increases. These changes indicate a growing prevalence of ASCSP-type solvation sheaths at higher Zr^{4+} concentrations (Supplementary Fig. 17), a trend further supported by Fourier transform infrared (FTIR) spectroscopy and X-ray pair distribution function (PDF) analyses (Supplementary Figs. 18 and 19).

Ab initio molecular dynamics (AIMD) simulations reveal the molecular-level evolution of solid solvation structures. For simplicity, $ZrCl_4$ is used as a substitute for $Li_{3-x}In_{1-x}Zr_xCl_6$ as both exhibit the same dissolution behaviour in theory. The simulated coordination numbers of Zr^{4+} with O and Cl atoms within the inner solvation sheath (<3 Å) follow a trend that is consistent with experimental observations (Fig. 1f,b, Supplementary Fig. 20 and Supplementary Table 2). Electrostatic potential (ESP) calculations further illustrate the electron redistribution during evolution of the solvation structure (Supplementary Fig. 21 and Supplementary Table 3). As the structure changes from CSA-type to ASCSP-type, the electron density decreases at the o-TCBQ aromatic ring and increases at the Cl ligands coordinated to the Zr^{4+} cation. This charge transfer from organic to inorganic ligands lowers the electron density around the carbonyl groups in o-TCBQ, correlating with a gradual rise in the average working voltage. Thus, forming ASCSP-type inner solvation structures is essential for achieving high-voltage OEMs in solid cathode solutions.
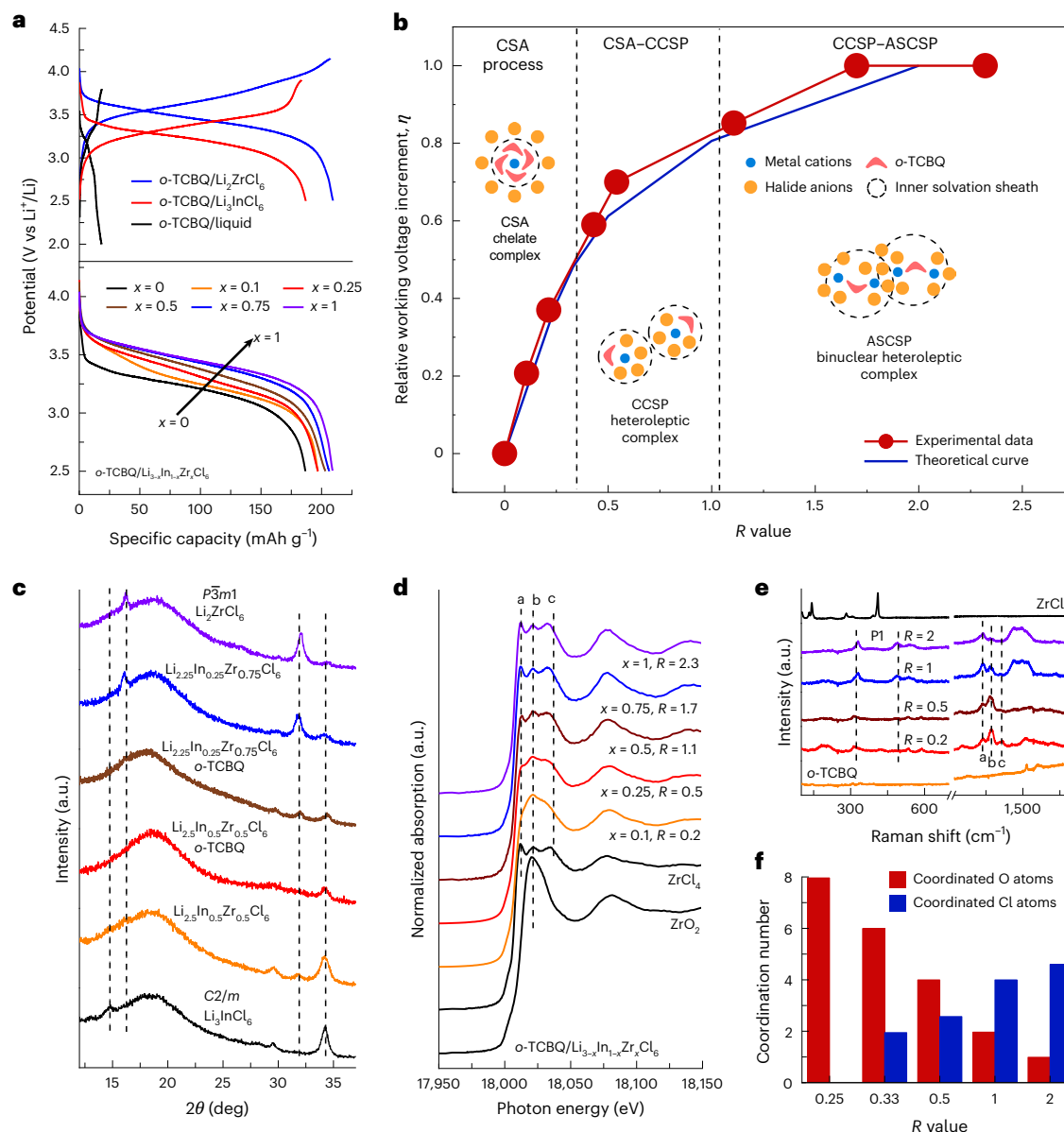
Fig. 1 | Evolution of solid solvation structure and its impact on the working voltage of the o-TCBQ solvent. a, Galvanostatic charge–discharge curves of o-TCBQ using a liquid electrolyte, Li_3InCl_6, Li_2ZrCl_6 and $Li_{3-x}In_{1-x}Zr_xCl_6$ solid electrolytes at 60 °C. **b**, Experimental and theoretical relationship between the relative working voltage increment η and the R value. **c**, XRD patterns of $Li_{3-x}In_{1-x}Zr_xCl_6$ ($x = 0$, 0.5, 0.75, 1) solid electrolytes and $Li_{3-x}In_{1-x}Zr_xCl_6$ ($x = 0.5$, 0.75) cathode solutions. **d**, Zr K-edge XANES spectra of $ZrCl_4$, ZrO_2 and $Li_{3-x}In_{1-x}Zr_xCl_6$ cathode solutions. **e**, Raman spectra of $ZrCl_4$, o-TCBQ and Zr^{4+}-based cathode solutions with increasing Zr^{4+} concentrations. **f**, Coordination number of Zr-O and Zr-Cl in the inner solvation sheath of Zr^{4+}-based cathode solutions with increasing Zr^{4+} concentrations extracted from AIMD simulations.

Rational design of solid solvation structures

The enhanced working voltage of o-TCBQ in Zr^{4+}-based cathode solutions motivates the exploration of alternative solid solutes to elevate its working voltage further. Homogeneous $Li_{3(1-x)}In_{1-x}M_xCl_{6+(y-6)x}$ ($0 \leq x \leq 0.667$; $3 \leq y \leq 5$) solid cathode solutions containing different metal cations (M^{y+} = Y^{3+}, Sc^{3+}, Zr^{4+}, Al^{3+}, Nb^{5+}) were constructed to investigate the impact of different cations on the average working voltage of o-TCBQ (Methods; Supplementary Figs. 22 and 23). For consistency, the R value for the different solid cathode solutions is fixed at unity and the testing temperature is set at 60 °C to minimize the influence of the varying ionic conductivity. As a result, the average working voltage of the o-TCBQ solvent increases from 3.30 V to 3.55 V (Fig. 2a). Meanwhile, in the FTIR spectra the asymmetric stretching vibration peak 'a' of the carbonyl group of o-TCBQ is redshifted from 1,678 to 1,585 cm^{-1} (Fig. 2b), indicating a progressive decrease in electron density at the carbonyl

group. To quantify the relationship between the M^{y+} cations and the average working voltage, we introduce the ionic potential ψ ($\psi = n/r$, where n is the charge number and r is the ionic radius) as a descriptor of the cation polarization strength. A clear linear correlation is observed, indicating that M^{y+} cations with a higher ionic potential enhance the working voltage of o-TCBQ, accompanied by a concurrent decrease in electron density at the carbonyl group (Fig. 2c). This trend identifies the Nb^{5+}-based cathode solution as the most promising system for achieving the highest working voltage. However, the highly covalent nature of Nb–Cl bonds limits the solubility of $NbCl_5$ in o-TCBQ, restricting the Nb^{5+} concentration beyond $R > 1$ and preventing the formation of the optimal ASCSP-type inner solvation sheath (Supplementary Fig. 24)[30]. Quantitative Nb K-edge XANES analysis and AIMD simulations confirm that the saturated Nb^{5+}-based cathode solution adopts a CCSP-type solvation structure (Supplementary Figs. 25 and 26). Overcoming this
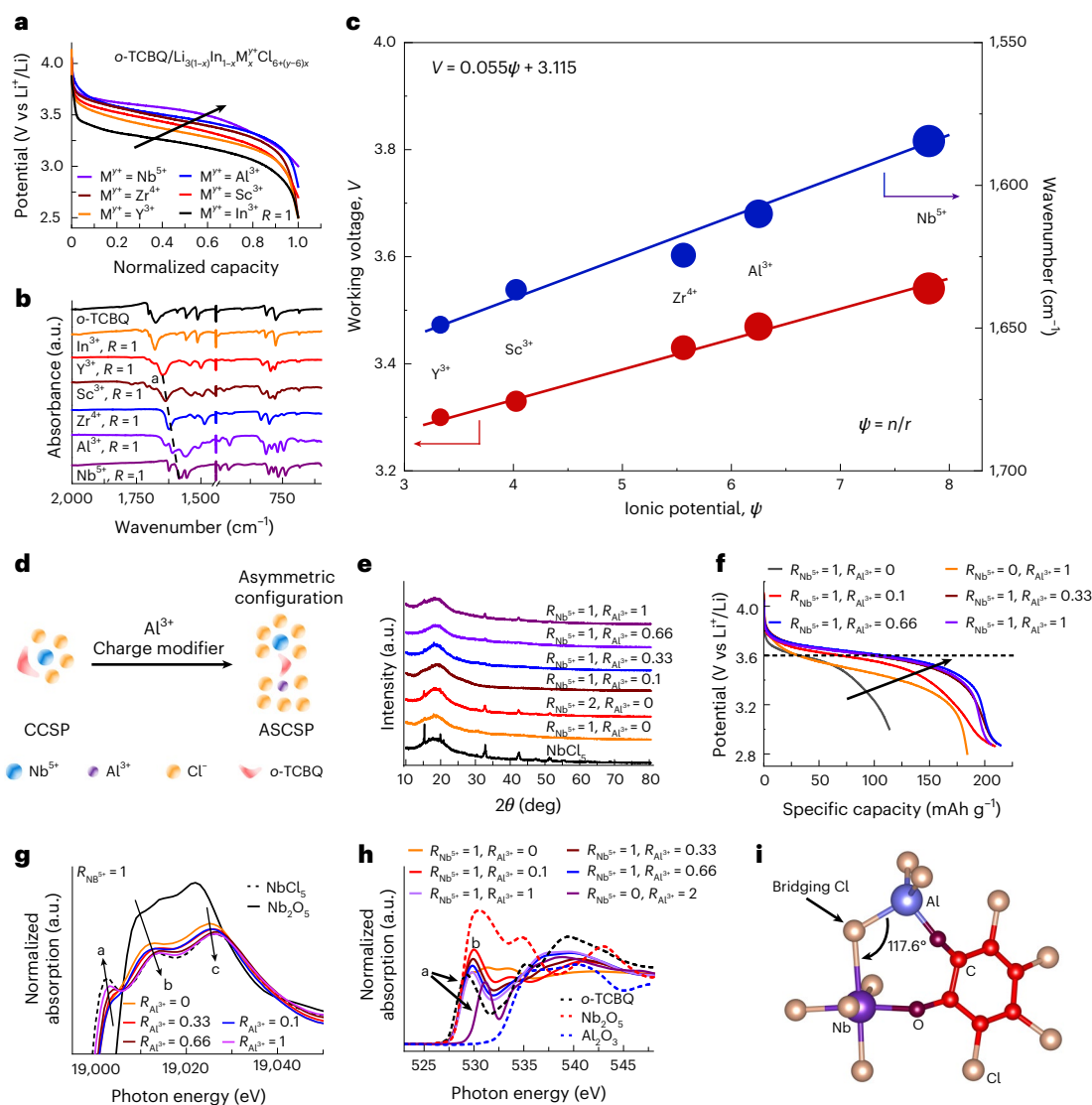
Fig. 2 | Structures and properties of various solid solvation structures.
a,b, Galvanostatic discharge curves of $Li_{3(1-x)}In_{1-x}M_xCl_{6+(y-6)x}$ (M^{y+} = Y^{3+}, Sc^{3+}, Zr^{4+}, Al^{3+}, Nb^{5+}; $0 \le x \le 0.667$; $3 \le y \le 5$) cathode solutions at 60 °C (**a**) and the corresponding FTIR spectra (**b**). **c**, Linear relationship between the ionic potential of the cations (ψ) and the working voltage/wavenumber (characteristic peak of the C=O bond) of the o-TCBQ solvent. **d**, Schematic illustration of designing ASCSP-type asymmetric inner solvation sheath. **e**, XRD patterns of Nb^{5+}/Al^{3+}-based solid cathode solutions with different concentrations. **f**, Galvanostatic discharge curves of Nb^{5+}/Al^{3+}-based solid cathode solutions at RT (60 °C for pure Nb^{5+}-based (R_{Nb5+} = 1) and Al^{3+}-based (R_{Al3+} = 0) solid cathode solutions). **g,h**, Nb K-edge XANES spectra (R_{Nb5+} = 1) (**g**) and O K-edge XANES spectra of Nb^{5+}/Al^{3+}-based solid cathode solutions (**h**). **i**, Representative asymmetric ASCSP-type solvation structure in Nb^{5+}/Al^{3+}-based solid cathode solutions (R_{Al3+} = 1) extracted from AIMD simulations.

solubility barrier is therefore critical for enabling ASCSP-type solvation and unlocking the full voltage potential of o-TCBQ in the Nb^{5+}-based cathode solution.

Inspired by the use of NaCl as a surface-charge modifier to enhance protein solubility in water[31], we introduce a second cation, Al^{3+}, as a charge-modifying agent to construct asymmetric Nb^{5+}/Al^{3+}-based cathode solutions with heteronuclear heteroleptic structures (Fig. 2d). This strategy successfully enables the formation of an ASCSP-type inner solvation sheath around the Nb^{5+} cations. The selection of Al^{3+} is guided by two key criteria: (1) its high solubility in the o-TCBQ solvent (Supplementary Fig. 27) and (2) its high ionic potential ψ (Fig. 2c). XRD patterns confirm a consistently amorphous structure across various Al^{3+} concentrations (Fig. 2e), indicating the effective dissolution of both Nb^{5+} and Al^{3+} cations in the o-TCBQ solvent. As a result, the working voltage of the o-TCBQ solvent increases progressively with rising Al^{3+} concentration (Fig. 2f), reaching a peak value of 3.6 V vs Li$^+$/Li at RT when R_{Al3+} ranges from 0.33 to 1 (Supplementary Fig. 28). Spectroscopic

characterization combined with AIMD simulations confirm the formation of an asymmetric ASCSP-type inner solvation sheath in Nb^{5+}/Al^{3+}-based solid cathode solutions. Nb K-edge XANES spectra show an increased intensity of peak 'a' and a concurrent decrease in peaks 'b' and 'c' with increasing Al^{3+} concentration (Fig. 2g). This spectral evolution, from resembling Nb$_2$O$_5$ to more closely matching NbCl$_5$, indicates a progressively Cl$^-$-anion-dominated coordination environment around Nb, consistent with ASCSP-type solvation. Similar trends are observed in Nb K-edge EXAFS spectra (Supplementary Fig. 29). O K-edge XANES spectra reveal distinct features for Nb^{5+}/Al^{3+}-based cathode solutions compared with pure Nb^{5+}-based or Al^{3+}-based cathode solutions (Fig. 2h), highlighting substantial differences in their electronic structures. Peak 'a' corresponds to the $s \rightarrow \pi^*$ transitions in the o-TCBQ solvent. Peak 'b' ($1s \rightarrow 4pd$), associated with Nb–O hybridization, progressively weakens, and the emergence of broad features between 535 and 545 eV, which resemble those of Al–O interactions in the ASCSP-type inner solvation sheaths of pure Al^{3+}-based cathode

solutions, indicates the formation of the ASCSP-type solvation sheath around both Nb^{5+} and Al^{3+} cations with increasing Al^{3+} concentration. Meanwhile, Al K-edge XANES spectra shows a similar trend (Supplementary Fig. 30). The evolution of the solid solvation structure with increasing Al^{3+} concentration is further corroborated by Raman, FTIR and PDF analyses (Supplementary Figs. 31–33). Finally, AIMD simulations of Nb^{5+}/Al^{3+}-based cathode solutions ($R_{Nb^{5+}} = 1$; $R_{Al^{3+}} = 1$) confirm the asymmetric ASCSP-type inner solvation sheath, revealing bridging Cl atoms connecting Nb^{5+} and Al^{3+} centres via Nb–Cl–Al motifs with a bond angle of 117.6° (Fig. 2i).

Redox chemistry in the asymmetric inner solvation sheath

At RT, the o-TCBQ solvent exhibits a large voltage hysteresis (≈700 mV) and a limited discharge capacity (≈150 mAh g^{-1}) in pure Nb^{5+}-based cathode solutions, whereas it shows minimal hysteresis and a high reversible capacity in asymmetric Nb^{5+}/Al^{3+}-based cathode solutions (Fig. 3a). This improved performance arises from the unique equilibrium redox pathway enabled by the asymmetric inner solvation sheath, which promotes a flat voltage plateau, low hysteresis and enhanced redox activity (Fig. 3b). In solid solvation structures composed of heteroleptic complexes, electron transfer from the o-TCBQ ligand to Cl ligands via metal cations—a process that we term ligand-to-metal-to-ligand charge transfer (LMLCT)—is essential for dissipating electron density from the carbonyl groups of o-TCBQ, thus enabling high redox potential and fast kinetics. This process depends crucially on the nature of the M–Cl bond. In pure Nb^{5+}-based cathode solutions, strong covalent Nb–Cl bonds, arising from intense d–p hybridization, hinder charge transfer from the Nb d orbitals to the Cl ligands. As a result, the Nb d orbitals become oversaturated during discharge, leading to electron accumulation at the carbonyl group of o-TCBQ and suppressing further reduction. We call this phenomenon the 'non-equilibrium redox pathway' (Supplementary Fig. 34). By contrast, the asymmetric configuration in Nb^{5+}/Al^{3+}-based cathode solutions activates the LMLCT process as the weaker covalent nature of Al–Cl bonds facilitates efficient electron transfer. During discharge, excess charge localized on Nb-coordinated carbonyl groups is redistributed to Al-coordinated sites, establishing an 'equilibrium redox pathway' (Supplementary Fig. 34). This asymmetric configuration alleviates the Nb d-orbital saturation observed in pure Nb^{5+}-based cathode solutions, stabilizes intermediate states and enables fast redox kinetics (~180 mV) along with nearly complete two-electron redox activity at RT (Fig. 3a). A similar ligand-to-metal charge-transfer mechanism has also been reported in lithium-rich layered oxides, where it regulates both cationic and anionic redox reactions[32–34].

The ex situ Cl K-edge XAS spectra of pure Nb^{5+}-based and asymmetric Nb^{5+}/Al^{3+}-based cathode solutions provide direct evidence that supports the LMLCT process during the equilibrium redox pathway of o-TCBQ in the asymmetric solvation sheath (Fig. 3c). The pre-edge peak 'a' corresponds to the excitation of Cl atoms from the occupied 1s state to unoccupied pd hybridization states between Nb and Cl atoms. During discharge, the intensity of peak 'a' decreases monotonically in pure Nb^{5+}-based cathode solutions, indicating the gradual saturation of the pd hybridization states. By contrast, in the Nb^{5+}/Al^{3+}-based cathode solutions, the evolution of peak 'a' follows a different pattern: initially, its intensity decreases due to charge transfer from the o-TCBQ ligand to the empty pd hybridization orbitals. As discharge progresses, the intensity then increases even beyond the initial value, due to the charge transfer from the saturated pd hybridization orbitals between the Nb and Cl atoms to the Cl ligands coordinated with the Al^{3+} cation. The pre-edge feature 'b' reflects the excitation of the Cl atoms from the occupied 1s state to unoccupied pd hybridization states between the In and Cl atoms, which follows a trend similar to peak 'a' in both the pure Nb^{5+}-based and Nb^{5+}/Al^{3+}-based cathode solutions. ESP calculations further validate the activation of the LMLCT process in the asymmetric

solvation sheath (Fig. 3d,e and Supplementary Table 4). To simulate the discharge process, one and two electrons were sequentially introduced into the pristine models. In the pure Nb^{5+}-based cathode solution, electron density accumulates predominantly around the Nb centre upon reduction, indicating progressive saturation of its d orbitals. Consequently, the O atoms in o-TCBQ exhibit significantly higher electron density than the Cl atoms coordinated with the Nb^{5+} cations, reflecting the suppression of the charge transfer process. By contrast, in the Nb^{5+}/Al^{3+}-based cathode solution, electrons localize on Cl atoms coordinated with the Al^{3+} cations after two-electron reduction, whereas the Nb centre is less saturated than in the pure Nb^{5+} system, providing strong evidence of an activated LMLCT process. These computed electron distributions, corroborated by spectroscopic data, demonstrate that the LMLCT process facilitates the redox activity of o-TCBQ within the asymmetric inner solvation sheath, underscoring its important role in the design of solid solvation structures.

Electrochemical performance of ASSBs

All of the electrochemical data were collected using home-made model cells under a low stack pressure (≈7 MPa) at RT (Supplementary Fig. 35). The galvanostatic charge–discharge curve of the o-TCBQ solvent shows a high average working voltage of 3.6 V vs. Li^+/Li and a high discharge capacity of 211 mAh g^{-1} at 0.1C, demonstrating the superior gravimetric energy-storage metrics compared with conventional inorganic cathodes such as $LiNi_{0.5}Mn_{0.3}Co_{0.2}O_2$ (NCM523) (3.8 V, ~160 mAh g^{-1}) or $LiFePO_4$ (3.45 V, ~170 mAh g^{-1}) (Fig. 4a), and even verging on the realm of state-of-the-art nickel-rich TMOs ($LiNi_{0.83}Co_{0.11}Mn_{0.06}O_2$ (NCM83)) (Supplementary Fig. 36). The high working voltage of the o-TCBQ solvent in asymmetric Nb^{5+}/Al^{3+}-based cathode solutions also demonstrates an excellent value for n-type OEMs in both liquid and solid cells, leading to an exceptional energy density of 760 Wh kg^{-1} (calculated based on active materials) (Fig. 4b). Moreover, the o-TCBQ solvent also displays a high-rate capability at RT (Fig. 4c and Supplementary Fig. 37). At a moderate current density of 0.5C, the overall discharge capacity shows negligible fading compared with the cells operated at a low current density of 0.1C (Supplementary Fig. 38). At high current densities of 2C, 5C and 10C, the attainable discharge capacities could reach 150, 99 and 55 mAh g^{-1}, respectively. Such an excellent rate performance originates from the in-situ-formed electronic/ionic percolation network in Nb^{5+}/Al^{3+}-based solid cathode solutions. As for cycling tests at current densities of 0.1 and 0.5C, the ASSBs demonstrate a high capacity retention of 82 and 90%, respectively, after 200 cycles (Fig. 4d). The initial capacity increase within the first 50 cycles arises from dynamically improved interfacial contact in the ASSBs, which will be discussed in detail in the next section. To demonstrate their practical viability, ASSBs with high active material mass loadings of 8 and 17 mg cm^{-2} were fabricated. A high areal capacity of 1.5 and 3.1 mAh cm^{-2}, respectively (Fig. 4e) and a notable capacity retention of 94 and 77% can be achieved after 100 cycles (Fig. 4f and Supplementary Fig. 39). Furthermore, the long-term cycling stability of the ASSBs was validated under high current densities of 1C, 5C and 10C (Fig. 4g,h). The corresponding capacity retention values are as high as 70, 85 and 100% after 3,000, 7,570 and 6,100 cycles, respectively. In addition, ASSBs tested with a Li-metal anode could also deliver a stable cycling profile at a rate of 1C (Supplementary Fig. 40). By optimizing the particle size of o-TCBQ and the halide electrolyte, and incorporating the Ta-based $1.6Li_2O$-$TaCl_5$ (LTOC) halide electrolyte with ultrahigh ionic conductivity[35], the active o-TCBQ content in the cathode composites can be increased to 30% at RT (Supplementary Fig. 41). A comprehensive overview of the electrochemical performance using both typical TMOs and OEMs in ASSBs is conducted for comparison (Fig. 4i and Supplementary Table 5)[36–41]. In terms of cycle stability, lifespan, rate performance and operating temperature, the ASSBs presented in this work demonstrate one of the best results among the reported literature. Furthermore, the electrochemical performance in this study compares favourably with results for other organic small molecules as
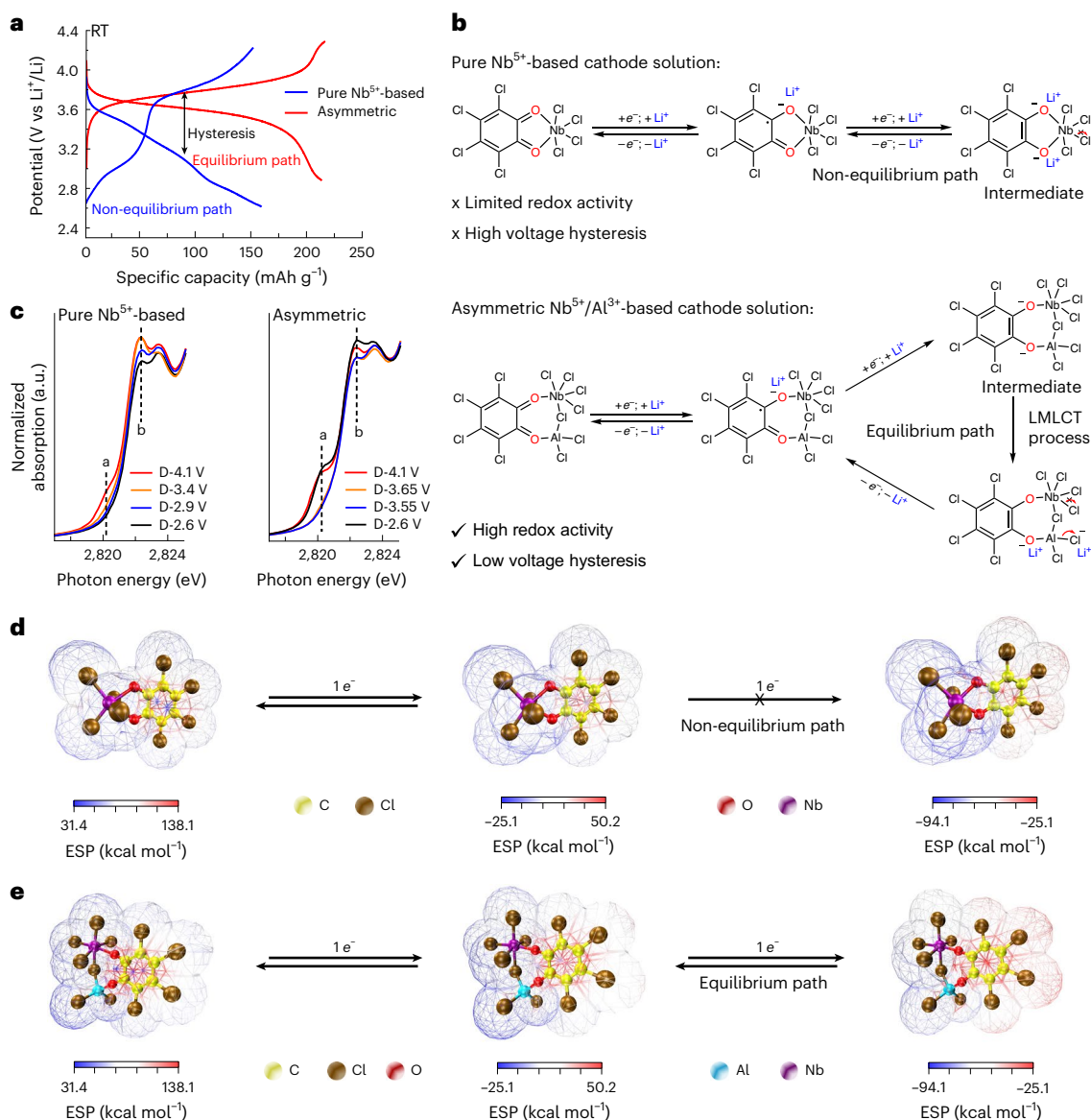
Fig. 3 | Non-equilibrium and equilibrium redox pathways of the *o*-TCBQ solvent in solid cathode solutions. a, Galvanostatic charge–discharge curves at RT, **b**, Schematic illustration of the redox chemistry of pure Nb⁵⁺-based (top) and asymmetric Nb⁵⁺/Al³⁺-based (bottom) cathode solutions. **c**, Ex situ Cl K-edge XAS spectra of pure Nb⁵⁺-based (left) and asymmetric Nb⁵⁺/Al³⁺-based (right) cathode solutions. 'D-' denotes discharged voltage of selecting points. **d,e**, ESP maps in pristine, one-electron and two-electron states of pure Nb⁵⁺-based cathode solutions (**d**) and asymmetric Nb⁵⁺/Al³⁺-based cathode solutions (**e**). *e⁻*, electron.

cathode materials in both liquid and all-solid-state lithium-ion batteries (Supplementary Table 6), demonstrating their potential for future use as high-performance, high-energy-density cathodes.

Self-healing interfaces

TMOs, such as NCM83, are the most widely used cathodes in current ASSBs. However, their substantial volumetric expansion (up to 20%) during (de)lithiation and rigid structures often lead to mechanical failure at the TMO/solid electrolyte interface during extended cycling (Fig. 5a)[42,43]. To maintain sufficient solid–solid contact, high uniaxial stack pressures (typically hundreds of megapascals) are required[41,44], which poses a huge barrier to the practical application of ASSBs. By contrast, our study demonstrates the low-stack-pressure operation (≈7 MPa) of high-performance ASSBs enabled by self-healing interfaces in asymmetric Nb⁵⁺/Al³⁺-based cathode solutions (Fig. 5a). During discharge, *o*-TCBQ gains electrons to form the electron-rich $[C_6O_2Cl_4]^{2-}$ moiety, which electrostatically interacts with M^{y+} cations in the halide electrolyte. This interaction provides the kinetic driving force for the

partial deformation of *o*-TCBQ. Notably, the low Young's modulus nature of OEMs (1–10 GPa) compared with rigid TMOs (100–1,000 GPa) provides the necessary prerequisites for solid-state diffusion[45]. This self-healing behaviour is reflected in the electrochemical performance, where a continuous increase in discharge capacity is observed during the initial cycles, eventually exceeding 200 mAh g⁻¹ and achieving high material utilization. Benefitting from self-healing interfaces, the *o*-TCBQ solvent exhibits both a higher capacity retention and a better rate capability (90%@1,000 cycles and 50%@5C, respectively) than NCM83 cathodes (66%@1,000 cycles; 20%@5C) under a low stack pressure of ≈7 MPa (Fig. 5b,c). In addition, these stable interfaces, formed through in situ interactions between *o*-TCBQ and the halide electrolytes, enable ASSBs to achieve a long calendar life with negligible deterioration after a two-month ageing test (Supplementary Fig. 42).

The interfacial characteristics within an asymmetric Nb⁵⁺/Al³⁺-based cathode solution and an NCM83 electrode are monitored via in situ electrochemical impedance spectroscopy (EIS) and corresponding distribution of relaxation times (DRT) analyses (Fig. 5d,e).
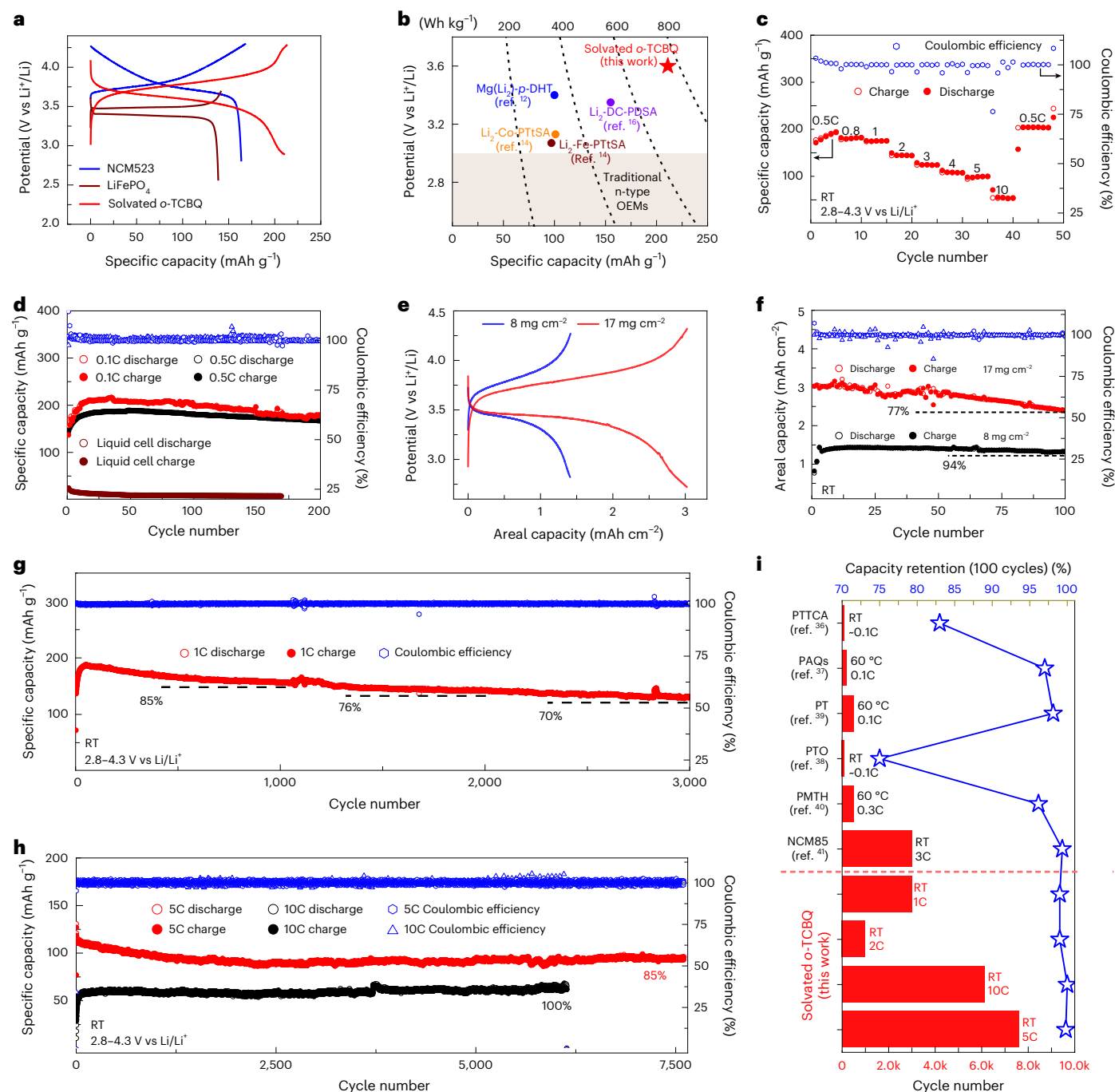
Fig. 4 | Electrochemical performance of *o*-TCBQ in asymmetric Nb^{5+}/Al^{3+}-based cathode solutions at RT. a, Galvanostatic charge–discharge curves of NCM523, LiFePO$_4$ and *o*-TCBQ at 0.1C (1C = 160/170/218 mAh g^{-1} for NCM523/LiFePO$_4$/*o*-TCBQ, respectively). **b**, Comparison of *o*-TCBQ with reported OEMs in the literature in terms of working voltage and energy density (calculated based on active materials). Mg(Li$_2$)-p-DHT, magnesium (2,5-dilithium-oxy)-terephthalate; Li$_2$-DC-PDSA, dilithium(2,5-dichloro-1,4-phenylene)bis((methylsulfonyl)amide); Li$_2$-Co-PTtSA, Li$_2$-Co-benzene-1,2,4,5-tetra-methylsulfonamide; Li$_2$-Fe-PTtSA, Li$_2$-Co-benzene-1,2,4,5-tetra-methylsulfonamide. **c**, Rate performance of *o*-TCBQ. **d**, Cycling performance of *o*-TCBQ at 0.1C and 0.5C. **e,f**, Galvanostatic charge–

discharge curves (**e**) and cycling performance of ASSBs with high areal capacity results (**f**). Current density values are 0.1C for the 8 mg cm^{-2} cell and 0.05C for the 17 mg cm^{-2} cell. **g,h**, Long-cycling profiles of *o*-TCBQ at 1C (**g**) and at 5C and 10C (**h**). **i**, Electrochemical performance comparison of cycle numbers (where k denotes ×1,000), capacity retention and operating temperature of *o*-TCBQ and representative ASSBs reported in the literature. PTTCA, poly(trithiocyanuric acid); PAQs, poly(anthraquinone); PT, 5,7,12,14-pentacenetetrone; PTO, pyrene-4,5,9,10-tetraone; PMTH, dipentamethylenethiuramhexasulfide; NCM85, LiNi$_{0.85}$Co$_{0.10}$Mn$_{0.05}$O$_2$.

In the NCM83 electrode, the emerging semicircle at mid-frequency associated with the charge-transfer resistance (R_{ct}) is observed during the charge–discharge process compared with the pristine electrode, indicating surface rupture and the formation of a rock salt phase on the surface of the NCM83 particles during cycling[46]. In addition, R_{ct} in the

NCM83 electrode exhibits fluctuating behaviour, initially decreasing and then increasing during the charge–discharge process due to the volumetric expansion of NCM83 (Supplementary Fig. 43 and Supplementary Table 7). By contrast, R_{ct} in the Nb^{5+}/Al^{3+}-based cathode solution remains largely unchanged throughout the cycling (Supplementary
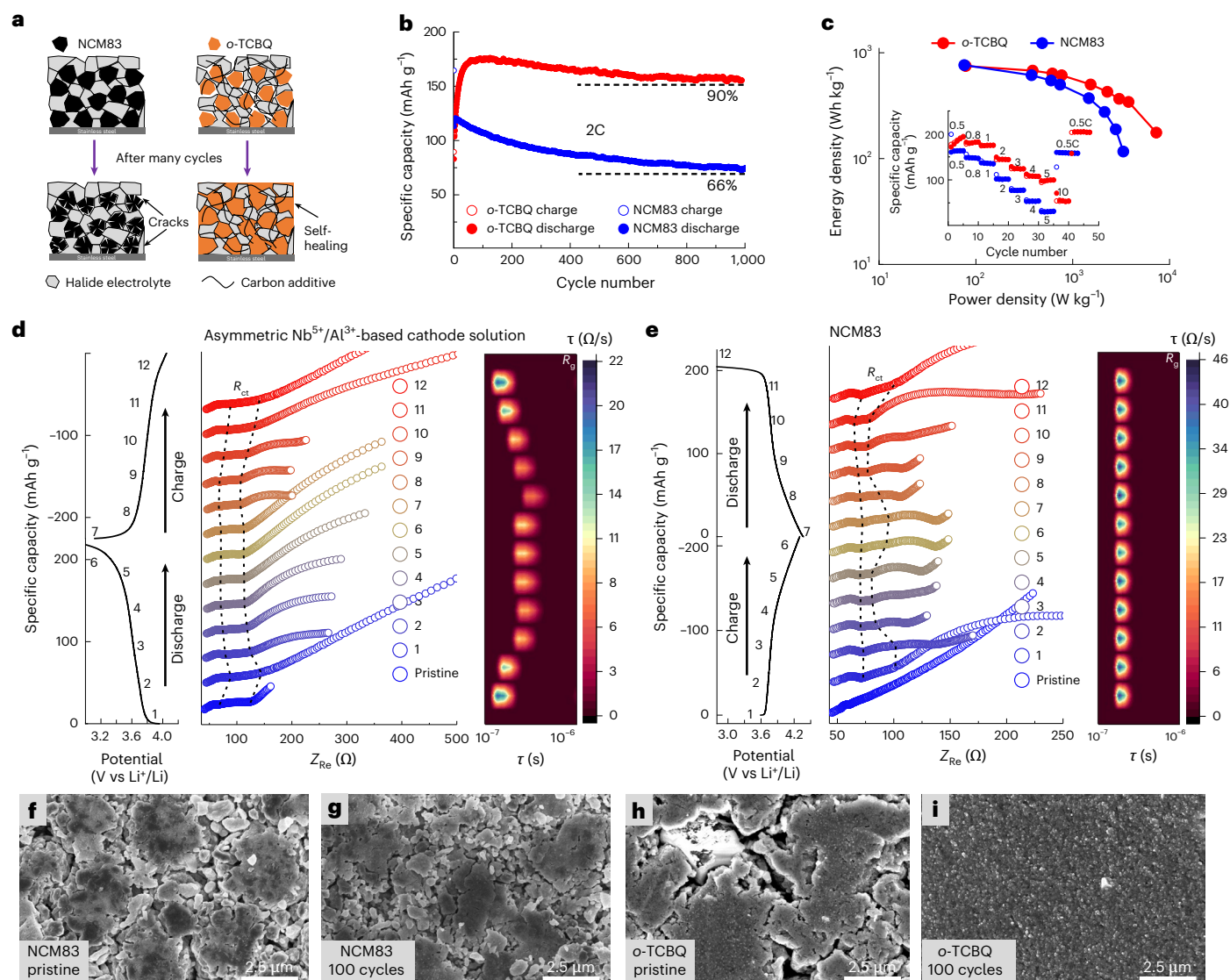
Fig. 5 | Interfacial evolution of NCM83 electrode and asymmetric Nb^{5+}/Al^{3+}-based cathode solutions. a, Schematic illustration of interfacial evolution in asymmetric Nb^{5+}/Al^{3+}-based cathode solutions (right) and NCM83 (left) during cycling. **b,c**, One-thousand-cycle comparison at the 2C rate (**b**) and a Ragone plot and rate comparison (inset) between the NCM83 electrode and *o*-TCBQ in an asymmetric Nb^{5+}/Al^{3+}-based cathode solution under a low stack pressure ($\approx$7 MPa) (**c**). **d,e**, In situ EIS Nyquist plots and the corresponding DRT contour plots with a time constant (τ) of between 10^{-7} and 10^{-6} s for an asymmetric Nb^{5+}/Al^{3+}-based cathode solution (**d**) and an NCM83 electrode (**e**) in the second cycle. **f–i**, SEM images of the NCM83 electrode (**f,g**) and an asymmetric Nb^{5+}/Al^{3+}-based cathode solution (**h,i**) before (**f,h**) and after (**g,i**) cycling.

Fig. 44 and Supplementary Table 8). Furthermore, the DRT peak corresponding to the grain boundary resistance (R_g), with a time constant (τ) between 10^{-7} and 10^{-6} s (ref. 47), shifts to a lower time constant and decreases in intensity during discharge in the Nb^{5+}/Al^{3+}-based cathode solution, before returning to its original state during charge. By contrast, the DRT peak in the NCM83 electrode shows minimal variation throughout the charge–discharge process. As τ in the DRT is only related to interfacial properties[48], the reversible variation of τ belonging to the grain boundary during a single charge–discharge cycle suggests the possible infiltration of *o*-TCBQ into the grain boundaries of the halide electrolyte during Li$^+$ insertion and extraction, thereby altering the grain boundary properties. With extended cycling, the continued increase in τ and decreased peak intensity indicate progressive infiltration (Supplementary Fig. 45a), enhancing the contact between the redox-active centres and the halide electrolytes. As a result, R_{ct} decreases from 180 to 20 Ω over 1,000 cycles in the Nb^{5+}/Al^{3+}-based cathode solution (Supplementary Fig. 45b), further supporting the presence of self-healing

interfaces. By contrast, R_{ct} increases from 20 to 80 Ω after just 100 cycles in the NCM83 electrode (Supplementary Fig. 45c), indicating severe mechanical failure under a low stack pressure.

Characterization via scanning electron microscopy (SEM) imaging provides a clear visualization of the microstructural evolution in both systems after cycling (Fig. 5f–i). In the SEM images of the NCM83 electrode, distinct NCM83 and halide electrolyte particles are differentiated by their contrasting textures, with microcracks developing inside the NCM83 particles after 100 cycles. Conversely, the SEM images of the Nb^{5+}/Al^{3+}-based cathode solution show several cracks in the pristine electrode, which, however, disappear entirely in the electrode after 100 cycles, revealing a highly uniform surface that underscores the benefits of self-healing interfaces. Energy-dispersive X-ray spectroscopy (EDS) mapping (Supplementary Fig. 46) further confirms the spatial distribution of *o*-TCBQ and halide electrolytes during extended cycling, validating the self-healing behaviour. In summary, beyond enabling high average working voltage for n-type OEMs, the in situ interactions

between OEMs and halide electrolytes contribute to ASSBs capable of long-term cycling stability at low stack pressures, offering a promising strategy for practical low-pressure ASSBs.

Conclusions

In conclusion, we report a solid-solvation-structure design strategy that enables a high working voltage and outstanding cycling stability for n-type organic small molecules in ASSBs. To unravel the underlying solid-state solvation chemistry, we systematically investigated the interplay between OEMs, halide electrolytes ($Li_{3(1-x)}In_{1-x}M_xCl_{6+(y-6)x}$; M^{y+} = Y^{3+}, Sc^{3+}, Zr^{4+}, Al^{3+}, Nb^{5+}; $0 \le x \le 0.667$; $3 \le y \le 5$) and their resulting solvation configurations. Using o-TCBQ and $Li_{3-x}In_{1-x}Zr_xCl_6$ halide electrolytes as the proof-of-concept solid solvent and solutes, respectively, we established a direct correlation between evolution of the solvation structure and the working voltage. From comprehensive screening of OEM–halide electrolyte combinations, we proposed preliminary criteria for selecting OEMs as solid solvents. Structural analyses and AIMD simulations revealed three distinct solvation sheath models (CSA, CCSP and ASCSP), with the ASCSP configuration proving most effective in boosting the working voltage. Guided by this insight, we optimized the inner solvation sheath via metal-cation substitution and asymmetric sheath design, achieving a working voltage of 3.6 V vs Li^+/Li for n-type OEMs, which is comparable to the state-of-the-art nickel-rich NCM83 cathode. Furthermore, we uncovered the charge-transfer mechanism from the o-TCBQ organic ligand to Cl inorganic ligands within the asymmetric inner solvation sheath, which brings about accelerated redox kinetics. Finally, the formation of self-healing interfaces facilitated an exceptional rate performance and cycling stability (>7,500 cycles) under a low stack pressure (≈7 MPa). This work offers a strategy for designing high-voltage, durable OEMs and provides opportunities for next-generation, cost-effective ASSBs.

Online content

Any methods, additional references, Nature Portfolio reporting summaries, source data, extended data, supplementary information, acknowledgements, peer review information; details of author contributions and competing interests; and statements of data and code availability are available at https://doi.org/10.1038/s41557-025-01866-0.

References

1. Williams, D., Byrne, J. & Driscoll, J. A high energy density lithium/dichloroisocyanuric acid battery system. *J. Electrochem. Soc.* **116**, 2 (1969).
2. Lu, Y. & Chen, J. Prospects of organic electrode materials for practical lithium batteries. *Nat. Rev. Chem.* **4**, 127–142 (2020).
3. Lu, Y., Zhang, Q., Li, L., Niu, Z. Q. & Chen, J. Design strategies toward enhancing the performance of organic electrode materials in metal-ion batteries. *Chem* **4**, 2786–2813 (2018).
4. Armand, M. et al. Conjugated dicarboxylate anodes for Li-ion batteries. *Nat. Mater.* **8**, 120–125 (2009).
5. Hu, J. et al. Emerging organic electrodes for Na-ion and K-ion batteries. *Energy Storage Mater.* **56**, 267–299 (2023).
6. Esser, B. et al. A perspective on organic electrode materials and technologies for next generation batteries. *J. Power Sources* **482**, 228814 (2021).
7. Luo, Y. et al. Application of polyaniline for Li-ion batteries, lithium–sulfur batteries, and supercapacitors. *ChemSusChem* **12**, 1591–1611 (2019).
8. Kye, H., Kang, Y., Jang, D., Kwon, J. E. & Kim, B.-G. p-Type redox-active organic electrode materials for next-generation rechargeable batteries. *Adv. Energy Sustain. Res.* **3**, 2200030 (2022).
9. Häupler, B., Wild, A. & Schubert, U. S. Carbonyls: powerful organic materials for secondary batteries. *Adv. Energy Mater.* **5**, 1402034 (2015).
10. Poizot, P. et al. Opportunities and challenges for organic electrodes in electrochemical energy storage. *Chem. Rev.* **120**, 6490–6557 (2020).
11. Liang, Y., Tao, Z. & Chen, J. Organic electrode materials for rechargeable lithium batteries. *Adv. Energy Mater.* **2**, 742–769 (2012).
12. Jouhara, A. et al. Raising the redox potential in carboxyphenolate-based positive organic materials via cation substitution. *Nat. Commun.* **9**, 4401 (2018).
13. Lakraychi, A. E. et al. An air-stable lithiated cathode material based on a 1,4-benzenedisulfonate backbone for organic Li-ion batteries. *J. Mater. Chem. A* **6**, 19182–19189 (2018).
14. Wang, J. et al. High performance Li-, Na-, and K-ion storage in electrically conducting coordination polymers. *Energy Environ. Sci.* **15**, 3923–3932 (2022).
15. Gottis, S., Barrès, A.-L., Dolhem, F. & Poizot, P. Voltage gain in lithiated enolate-based organic cathode materials by isomeric effect. *ACS Appl. Mater. Interfaces* **6**, 10870–10876 (2014).
16. Wang, J. et al. Conjugated sulfonamides as a class of organic lithium-ion positive electrodes. *Nat. Mater.* **20**, 665–673 (2021).
17. Song, Z., Qian, Y., Zhang, T., Otani, M. & Zhou, H. Poly(benzoquinonyl sulfide) as a high-energy organic cathode for rechargeable Li and Na batteries. *Adv. Sci.* **2**, 1500124 (2015).
18. Miroshnikov, M. et al. Power from nature: designing green battery materials from electroactive quinone derivatives and organic polymers. *J. Mater. Chem. A* **4**, 12370–12386 (2016).
19. Song, Z. P. et al. A quinone-based oligomeric lithium salt for superior Li–organic batteries. *Energy Environ. Sci.* **7**, 4077–4086 (2014).
20. Peng, C. et al. Reversible multi-electron redox chemistry of π-conjugated N-containing heteroaromatic molecule-based organic cathodes. *Nat. Energy* **2**, 17074 (2017).
21. Hong, Y. et al. A universal small-molecule organic cathode for high-performance Li/Na/K-ion batteries. *Energy Storage Mater.* **52**, 61–68 (2022).
22. Zhao, Q. et al. Oxocarbon salts for fast rechargeable batteries. *Angew. Chem. Int. Ed.* **55**, 12528–12532 (2016).
23. Wang, S. et al. Organic $Li_4C_8H_2O_6$ nanosheets for lithium-ion batteries. *Nano Lett.* **13**, 4404–4409 (2013).
24. Bhosale, M. E., Chae, S., Kim, J. M. & Choi, J.-Y. Organic small molecules and polymers as an electrode material for rechargeable lithium ion batteries. *J. Mater. Chem. A* **6**, 19885–19911 (2018).
25. Li, X. et al. Water-mediated synthesis of a superionic halide electrolyte. *Angew. Chem. Int. Ed.* **58**, 16427–16432 (2019).
26. Wang, C. et al. A universal wet-chemistry synthesis of solid-state halide electrolytes for all-solid-state lithium-metal batteries. *Sci. Adv.* **7**, eabh1896 (2021).
27. Driscoll, D. M. et al. Emergent solvation phenomena in non-aqueous electrolytes with multiple anions. *Chem* **9**, 1955–1971 (2023).
28. Helm, B. et al. Exploring aliovalent substitutions in the lithium halide superionic conductor $Li_{3-x}In_{1-x}Zr_xCl_6$ ($0 \le x \le 0.5$). *Chem. Mater.* **33**, 4773–4782 (2021).
29. Chen, S. et al. Enabling ultrafast lithium-ion conductivity of Li_2ZrCl_6 by indium doping. *Chin. Chem. Lett.* **33**, 4635–4639 (2022).
30. Sheckelton, J. P., Plumb, K. W., Trump, B. A., Broholm, C. L. & McQueen, T. M. Rearrangement of van der Waals stacking and formation of a singlet state at $T=90$ K in a cluster magnet. *Inorg. Chem. Front.* **4**, 481–490 (2017).
31. Hassan, S. A. Amino acid side chain interactions in the presence of salts. *J. Phys. Chem. B* **109**, 21989–21996 (2005).
32. House, R. A. et al. Delocalized electron holes on oxygen in a battery cathode. *Nat. Energy* **8**, 351–360 (2023).

33. House, R. A. et al. The role of O_2 in O-redox cathodes for Li-ion batteries. *Nat. Energy* **6**, 781–789 (2021).

34. House, R. A. et al. Covalency does not suppress O_2 formation in *4d* and 5*d* Li-rich O-redox cathodes. *Nat. Commun.* **12**, 2975 (2021).

35. Zhang, S. et al. A family of oxychloride amorphous solid electrolytes for long-cycling all-solid-state lithium batteries. *Nat. Commun.* **14**, 3780 (2023).

36. Yang, Z. et al. Room-temperature all-solid-state lithium–organic batteries based on sulfide electrolytes and organodisulfide cathodes. *Adv. Energy Mater.* **11**, 2102962 (2021).

37. Ji, W. et al. A high-performance organic cathode customized for sulfide-based all-solid-state batteries. *Energy Storage Mater.* **45**, 680–686 (2022).

38. Zhang, J. et al. Microstructure engineering of solid-state composite cathode via solvent-assisted processing. *Joule* **5**, 1845–1859 (2021).

39. Zhou, X. et al. A highly stable Li–organic all-solid-state battery based on sulfide electrolytes. *Adv. Energy Mater.* **12**, 2103932 (2022).

40. Ji, W. et al. Practically accessible all-solid-state batteries enabled by organosulfide cathodes and sulfide electrolytes. *Adv. Funct. Mater.* **32**, 2202919 (2022).

41. Zhou, L. et al. High areal capacity, long cycle life 4 V ceramic all-solid-state Li-ion batteries enabled by chloride solid electrolytes. *Nat. Energy* **7**, 83–93 (2022).

42. Li, S. et al. Mutual modulation between surface chemistry and bulk microstructure within secondary particles of nickel-rich layered oxides. *Nat. Commun.* **11**, 4433 (2020).

43. Shishvan, S. S., Fleck, N. A., McMeeking, R. M. & Deshpande, V. S. Cracking and associated volumetric expansion of NMC811 secondary particles. *J. Power Sources* **588**, 233745 (2023).

44. Wang, K. et al. A cost-effective and humidity-tolerant chloride solid electrolyte for lithium batteries. *Nat. Commun.* **12**, 4410 (2021).

45. Hao, F. et al. Taming active material–solid electrolyte interfaces with organic cathode for all-solid-state batteries. *Joule* **3**, 1349–1359 (2019).

46. Streich, D. et al. Operando monitoring of early Ni-mediated surface reconstruction in layered lithiated Ni–Co–Mn oxides. *J. Phys. Chem. C* **121**, 13481–13486 (2017).

47. Lu, Y., Zhao, C.-Z., Huang, J.-Q. & Zhang, Q. The timescale identification decoupling complicated kinetic processes in lithium batteries. *Joule* **6**, 1172–1198 (2022).

48. Chen, J., Quattrocchi, E., Ciucci, F. & Chen, Y. Charging processes in lithium-oxygen batteries unraveled through the lens of the distribution of relaxation times. *Chem* **9**, 2267–2281 (2023).

Methods

Materials

All reagents are commercially available and were used as received. 3,4,5,6-Tetrachloro-1,2-benzoquinone (*o*-TCBQ; 97%), lithium chloride (LiCl; 99%), indium chloride (InCl$_3$; 98%), zirconium chloride (ZrCl$_4$; 99%), yttrium chloride (YCl$_3$; 99%), niobium chloride (NbCl$_5$; 99%), tantalum chloride (TaCl$_5$; 99%), aluminium chloride (AlCl$_3$; 99%), lithium oxide (Li$_2$O; 99%), lithium sulfide (Li$_2$S; 99%) and phosphorus pentasulfide (P$_2$S$_5$; 99%) were purchased from Sigma-Aldrich. Scandium chloride (ScCl$_3$; 99%) was purchased from Alfa Aesar. Bistrifluoromethanesulfonimide lithium salt (LiTFSI; 99%), 1,3-dioxolane (DOL; 99%) and ethylene glycol dimethyl ether (DME; 99%) were purchased from Shanghai Aladdin Bio-Chem Technology. NCM83 (particle size, ≈3 μm) and NCM523 (particle size, ≈3 μm) were obtained from China Automotive Battery Research Institute. Carbon black (Super P) and Ketjenblack (EC-600JD) were purchased from MSE Supplies. The high-energy planetary ball-milling machine (PM 200) was purchased from Retsch Mill.

Characterization

Laboratory-based XRD measurements were performed using a Bruker AXS D8 Advance instrument with Cu Kα radiation ($\lambda = 1.5406$ Å). To prevent the exposure of air-sensitive samples to air, Kapton tape was used to cover the sample holder. Raman spectra were measured using a HORIBA Scientific LabRAM HR Raman spectrometer operated under laser light at 532 nm. Cathode composites were attached to a carbon tape and covered by a transparent cover glass for testing. SEM and EDS images were obtained using a Thermo Scientific Helios 5 UX instrument. FTIR spectra were obtained using a Thermo Scientific Nicolet 6700 Analytical FTIR spectrometer with attenuated total reflection apparatus installed.

PDF data were collected at the Brockhouse High Energy Wiggler beamline of Canadian Light Source using a Varex XRD 4343CT area detector and a wavelength of 0.2114 Å. The samples were loaded into 0.8-mm-inner-diameter polyimide capillaries and sealed with epoxy in an argon-filled glovebox. XAS spectra were collected using the Hard X-ray Micro-Analysis (HXMA), Soft X-ray Microcharacterization Beamline (SXRMB) and Spherical Grating Monochromator (SGM) beamlines of Canadian Light Source. For the HXMA beamline, the samples were mixed with an appropriate amount of boron nitride and then pressed into pellets. Al-plastic bags were used for the air-sensitive samples. For the SXRMB and the SGM beamline, samples were spread on carbon tape and measured within a vacuum chamber. All XAS data were analysed using Athena software[49].

Synthesis of solid electrolytes

Synthesis of Li$_{3-x}$In$_{1-x}$Zr$_x$Cl$_6$ series solid electrolytes. LiCl, InCl$_3$ and ZrCl$_4$ were used as the precursors and mixed manually using an agate mortar according to a specific stoichiometric ratio. Then, the resulting powder (≈1 g) was placed in a zirconia jar (100 ml) with zirconia balls (40 g) in an argon-filled glovebox (H$_2$O < 0.1 ppm, O$_2$ < 0.1 ppm). For every high-energy ball-milling cycle, a 10 min ball-milling reaction at 500 revolutions per min (r.p.m.) and a 5 min rest period to allow natural cooling were applied. The total reaction time lasted 10 h to obtain the pure Li$_{3-x}$In$_{1-x}$Zr$_x$Cl$_6$ series solid electrolytes. The resulting products were transferred to a glovebox for further use.

Synthesis of Li$_6$PS$_5$Cl solid electrolyte. Li$_2$S, P$_2$S$_5$ and LiCl were used as the precursors (total amount ≈ 1 g) and placed in a zirconia jar (100 ml) with zirconia balls (40 g) according to the stoichiometric ratio. The mixture was ball-milled for 2 h at a speed of 200 r.p.m. and then vacuum sealed in quartz tubes for a further annealing process (550 °C for 5 h). The resulting product was transferred to a glovebox for further use.

Synthesis of 1.6Li$_2$O-TaCl$_5$ solid electrolyte. LiCl and TaCl$_5$ were used as the precursors and mixed manually using an agate mortar according to a specific stoichiometric ratio. Then, the resulting powder (≈1 g) was placed in a zirconia jar (100 ml) with zirconia balls (40 g) in an argon-filled glovebox (H$_2$O < 0.1 ppm, O$_2$ < 0.1 ppm). For every high-energy ball-milling cycle, a 10 min ball-milling reaction at 500 r.p.m. and a 5 min rest period for natural cooling were applied. The total reaction time lasted 10 h to obtain the pure LTOC powder. The resulting products were then transferred to a glovebox for further use.

Electrochemical measurements

Ionic conductivity testing. The ionic conductivities of the solid electrolytes were measured via potentiostat EIS using a VMP3 multichannel potentiostat 3/Z, with a frequency range of 7 MHz to 100 mHz and a voltage amplitude of 10 mV. For ionic conductivity testing, the solid electrolyte powder samples (≈120 mg) were cold-pressed into pellets (≈0.7 mm thickness; 1 mm diameter) under a pressure of ≈400 MPa using two stainless steel rods as the blocking electrode. To improve the contact between the solid electrolyte and stainless steel rods, carbon black (~5 mg) was spread on both sides of the solid electrolyte pellets before they were pressed together at a pressure of ≈200 MPa.

Preparation of cathode composites. To prepare various solid cathode solutions, *o*-TCBQ, MCl$_y$ (M^{y+} = Y^{3+}, Sc^{3+}, Zr^{4+}, Al^{3+}, Nb^{5+}), carbon black (Super P) and Li$_3$InCl$_6$ were used as the starting materials (total amount ≈ 200 mg) and placed in a zirconia jar (100 ml) with zirconia balls (40 g) at a specific molar ratio (*o*-TCBQ:Super P:MCl$_y$:Li$_3$InCl$_6$ = 2:2:*n*:6 − *n* weight ratio). The mixture was ball-milled at a speed of 350 r.p.m. for 5 h. Then, the resulting composites were transferred to a glovebox for further assembly. Li$_{3(1-x)}$In$_{1-x}$M$_x$Cl$_{6+(y-6)x}$ (M^{y+} = Y^{3+}, Sc^{3+}, Zr^{4+}, Al^{3+}, Nb^{5+}; 0 ≤ x ≤ 0.667; 3 ≤ y ≤ 5) solid electrolytes are obtained in situ during ball-milling. To prepare cathode composites with TMOs, NCM83/NCM523 and the Li$_3$InCl$_6$ solid electrolyte were mixed well using an agate mortar according to the 70:30 weight ratio. The resulting composites were then used directly for assembly without any additional treatment. To prepare the liquid battery, *o*-TCBQ, Ketjenblack and polyacrylonitrile copolymer binder (La133) were mixed well using an agate mortar according to the 60:30:10 weight ratio. The resulting slurry was cast onto Al foil (the Al foil was punched into Al discs with a diameter of 12 mm) and then dried in a vacuum oven at 100 °C for 24 h.

Assembly of ASSBs. First, a custom-made ceramic die with a diameter of 10 mm was used to press the Li$_3$InCl$_6$ solid electrolyte (120 mg) at ≈250 MPa for 2 min, forming a central solid electrolyte layer. Next, the cathode composite with NCM83/NCM523/*o*-TCBQ (10 mg) and the Li$_6$PS$_5$Cl solid electrolyte (40 mg) were spread over both sides of the Li$_3$InCl$_6$ central layer uniformly and pressed together at ≈500 MPa for another 3 min. The mass loading of *o*-TCBQ in the cathode solutions was in the range of 1.5–2.0 mg cm^{-2} for normal testing. For high-loading cells, the weight of the cathode composite with *o*-TCBQ was varied from 20 to 70 mg. On the anode side, home-made Li–In alloy (weight ratio 1:40) pieces were attached to the Li$_6$PS$_5$Cl surface and pressed together at ≈120 MPa to ensure intimate contact. For ASSBs using a Li-metal anode, Li metal was simply placed in contact with the Li$_6$PS$_5$Cl surface without any additional pressure. The galvanostatic charge/discharge tests were performed using a NEWARE CT-4008 battery testing system. All electrochemical tests for the ASSBs were carried out under a low stack pressure of ≈7 MPa.

Assembly of liquid cells. All half-cells were assembled as a CR2032 coin cell, with a polypropylene (Celgard 2400) membrane separator. To minimize the dissolution of *o*-TCBQ, a highly concentrated electrolyte of 5 M LiTFSI in DOL and DME with volume ratio of 1:1 was used. All cells were assembled in an argon-filled glovebox (H$_2$O, O$_2$ < 0.1 ppm). The mass loading of *o*-TCBQ on the electrode was in the

range of 1.5–2.0 mg cm^{-2}. The galvanostatic charge/discharge tests were performed using the NEWARE CT-4008 battery testing system.

In situ EIS and cyclic voltammetry tests. In situ EIS measurements were carried out using the VMP3 multichannel potentiostat 3/Z with a frequency range of 7 MHz to 100 mHz during the initial two cycles of the ASSBs. The cells were charged/discharged at a rate of 0.2C for 1 h, followed by a rest period of 0.5 h to reach equilibrium. DRT analysis using a MATLAB GUI toolbox developed by Ciucci and colleagues was conducted to extract the distribution of relaxation times in the EIS spectra[50]. Cyclic voltammograms of the ASSBs were obtained using the VMP multichannel potentiostat 3/Z at a scan rate of 0.1 mV s^{-1}.

Critical value of the solid-solvation-structure evolution model
The voltage of o-TCBQ is assumed to increase linearly with the R value in each solid solvation structure region of the cathode solutions, and the rate of voltage increase is determined by the average number of o-TCBQ coordinated with metal cations. Based on this assumption, the slope in the three solvation structure regions that represents the rate of voltage increase should satisfy the following relationship:

$$\frac{v_1}{u_1} \; : \; \frac{v_2 - v_1}{u_2 - u_1} \; : \; \frac{v_3 - v_2}{u_3 - u_2} = m_1 \; : \; m_2 \; : \; m_3,$$

where u_1, u_2 and u_3 are critical R values, v_1, v_2 and v_3 are critical η values, and m_1, m_2 and m_3 are average number of coordinated o-TCBQ with metal cations for each solvation structure, respectively. It is noteworthy that when introducing more solid solvation structures, the critical value of u_n and v_n can also be deducted based on the same method. Using the calculated values of v_1, v_2, v_n and so on, theoretical curves that represent the relationship between the relative working voltage increment (η) and the R value can be calculated, which are then compared with the experimental data for analysis (Supplementary Fig. 47).

AIMD simulations and ESP calculations
The AIMD simulations in this work were performed using the Vienna ab initio simulation package, version 5.4.1, within the projector augmented-wave approach, and the Perdew–Burke–Ernzerhof generalized gradient approximation functional was used as the exchange–correlation functional[51,52]. For the construction of each simulated cathode solution, we randomly disperse the corresponding proportions of metal halides and o-TCBQ molecules within a cubic box. The size of the cubic box was determined by the experimentally measured density of the cathode solution. Then, each system was equilibrated for 4 ps at 300 K in the canonical (*NVT*) ensemble. After that, a 15 ps AIMD simulation with a time step of 2 fs was performed on each system to trace the coordination situation. A Γ-point-only grid and a lower but sufficient energy cut-off of 280 eV were applied during the overall simulation process.

Static molecular calculations were performed using the Gaussian 16 package[53]. Hybrid density functional theory calculations were performed on all systems. The input model of each complex was based on the AIMD simulation results. The basis set 6-31G was used for Cl, C and O, and the basis set Lanl2mb was used for Al, Nb and Zr. The B3LYP functional was used for energy minimizations, frequency analyses and the evaluation of ESP of molecules. The charge analysis on each atom in different complexes and the ESP plots of the inner solvation structure complexes of Nb^{5+}/Al^{3+}-based and pure Nb^{5+}-based cathode solutions were realized using the Multiwfn package[54].

Data availability
The data that support the findings of this study are available within the Article and its Supplementary Information. Source data are provided with this paper.

References

49. Ravel, B. & Newville, M. ATHENA, ARTEMIS, HEPHAESTUS: data analysis for X-ray absorption spectroscopy using IFEFFIT. *J. Synchrotron Radiat.* **12**, 537–541 (2005).
50. Wan, T. H., Saccoccio, M., Chen, C. & Ciucci, F. Influence of the discretization methods on the distribution of relaxation times deconvolution: implementing radial basis functions with DRTtools. *Electrochim. Acta* **184**, 483–499 (2015).
51. Paier, J., Hirschl, R., Marsman, M. & Kresse, G. The Perdew–Burke–Ernzerhof exchange–correlation functional applied to the G2-1 test set using a plane-wave basis set. *J. Chem. Phys.* **122**, 234102 (2005).
52. Blöchl, P. E. Projector augmented-wave method. *Phys. Rev. B* **50**, 17953–17979 (1994).
53. Gaussian 16, Revision C.01 (Gaussian Inc., 2016).
54. Lu, T. & Chen, F. Multiwfn: a multifunctional wavefunction analyzer. *J. Comput. Chem.* **33**, 580–592 (2012).

Author contributions

Y.H. conceived the idea, collected the experimental data and drafted the raw manuscript; Y.H., H.S., J.F. and C.W. analysed the data and discussed the project; H.S. performed the AIMD simulations and DFT calculations. J.L., Q.Y., F.Z., W.L., S.D., Y.L., J.T.K., X.H., Y. Gao, M.J., X.L., Y.Z. and J.T. participated in discussions. Q.Y., Y.Y., Y. Gan, Y.W., N.C., M.S., T.P. and N.Z. collected the synchrotron data. H.S., J.F. and C.W. helped to revise the manuscript. X.S. supervised the whole project.

Competing interests

The authors declare no competing interests.

Additional information

Supplementary information The online version contains supplementary material available at https://doi.org/10.1038/s41557-025-01866-0.

Correspondence and requests for materials should be addressed to Changhong Wang or Xueliang Sun.

Peer review information *Nature Chemistry* thanks Yan Yao and the other, anonymous, reviewer(s) for their contribution to the peer review of this work.

Reprints and permissions information is available at www.nature.com/reprints.